



Brain tumor detection using statistical and machine learning method

Javaria Amin^a, Muhammad Sharif^{a,*}, Mudassar Raza^a, Tanzila Saba^b,
Muhammad Almas Anjum^c

^a Department of Computer Science, COMSATS University Islamabad, Wah Campus, GT Road Wah Cantt, Punjab 47040, Pakistan

^b College of Computer and Information Sciences, Prince Sultan University, Riyadh, 11586 Saudi Arabia

^c College of EME, NUST, Islamabad, Pakistan



ARTICLE INFO

Article history:

Received 22 September 2018

Revised 15 April 2019

Accepted 16 May 2019

Keywords:

Fused features

LBP

Pixel based results

PF clustering

Weiner Filter

ABSTRACT

Background and Objective: Brain tumor occurs because of anomalous development of cells. It is one of the major reasons of death in adults around the globe. Millions of deaths can be prevented through early detection of brain tumor. Earlier brain tumor detection using Magnetic Resonance Imaging (MRI) may increase patient's survival rate. In MRI, tumor is shown more clearly that helps in the process of further treatment. This work aims to detect tumor at an early phase.

Methods: In this manuscript, Weiner filter with different wavelet bands is used to de-noise and enhance the input slices. Subsets of tumor pixels are found with Potential Field (PF) clustering. Furthermore, global threshold and different mathematical morphology operations are used to isolate the tumor region in Fluid Attenuated Inversion Recovery (Flair) and T2 MRI. For accurate classification, Local Binary Pattern (LBP) and Gabor Wavelet Transform (GWT) features are fused.

Results: The proposed approach is evaluated in terms of peak signal to noise ratio (PSNR), mean squared error (MSE) and structured similarity index (SSIM) yielding results as 76.38, 0.037 and 0.98 on T2 and 76.2, 0.039 and 0.98 on Flair respectively. The segmentation results have been evaluated based on pixels, individual features and fused features. At pixels level, the comparison of proposed approach is done with ground truth slices and also validated in terms of foreground (FG) pixels, background (BG) pixels, error region (ER) and pixel quality (Q). The approach achieved 0.93 FG and 0.98 BG precision and 0.010 ER on a local dataset. On multimodal brain tumor segmentation challenge dataset BRATS 2013, 0.93 FG and 0.99 BG precision and 0.005 ER are acquired. Similarly on BRATS 2015, 0.97 FG and 0.98 BG precision and 0.015 ER are obtained. In terms of quality, the average Q value and deviation are 0.88 and 0.017. At the fused feature based level, specificity, sensitivity, accuracy, area under the curve (AUC) and dice similarity coefficient (DSC) are 1.00, 0.92, 0.93, 0.96 and 0.96 on BRATS 2013, 0.90, 1.00, 0.97, 0.98 and 0.98 on BRATS 2015 and 0.90, 0.91, 0.90, 0.77 and 0.95 on local dataset respectively.

Conclusion: The presented approach outperformed as compared to existing approaches.

© 2019 Published by Elsevier B.V.

1. Introduction

The brain is a complex human body organ and works through billions of cells. Brain tumors are caused due to the uncontrolled growth of cells. These cells might affect normal brain activities and also destroy normal cells [1,2]. Gliomas are a primary type of brain tumors. It contains IV grades (I, II: High Grade (HG) and III, IV: Low Grade (LG)) [3]. Despite major developments in the medical field like surgical procedure, chemotherapy and radiotherapy, still malignant brain tumor cases are untreatable. According to reports,

brain tumor is the 5th primary reason for the death of women from twenty to thirty nine years [4].

MRI is particularly helpful to validate gliomas because it gives detailed structure about the human brain [5]. For the brain analysis, T1c, T1, Flair and T2 are the most commonly used MRI sequences. These sequences provide different information related to the brain tumor. MRI test is based on radio frequency (RF) in which time of repetition (TR) and time of echo (TE) is calculated. T1c and T1 MRI are produced through short TR and TE time and cerebrospinal fluid (CSF) is dark in these sequences. CSF is colorless found in brain/ spinal cord. T2 MRI is produced by larger TR and TE time; therefore, CSF is bright in this modality. Flair is produced through very large TR and TE time; hence abnormal region remains bright and CSF is dark [6]. T2 is more sensitive to water content and more suitable for the abnormal region where water

* Corresponding author.

E-mail addresses: muhammadsharifmalik@yahoo.com (M. Sharif), tsaba@psu.edu.sa (T. Saba).

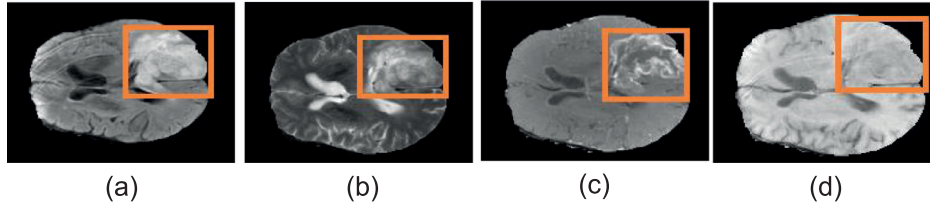


Fig. 1. Four imaging sequences: (a) Flair MRI (b) T2 MRI (c) T1 MRI (d) T1c MRI.

accumulates inside tissues of the brain. Flair provides more clear differentiation between the abnormal region and CSF as compared to other modalities (Fig. 1).

For brain tumor detection, accurate segmentation is a crucial process. The manual segmentation is time consuming for the radiologist [7] and hence, automated/ semi-automated techniques are required for precise tumor detection [8,9]. Nowadays fully automated methods [10] for classification between the tumor and non-tumor MRI [11] are common for clinical and research studies. These methods can provide more help to analyze the tumor region [12] and are developed rapidly in the last ten years [13]. Therefore, radiologists assume that computerized methods can improve their diagnosis abilities on the basis of automated machine learning methods [14–17]. Despite more efforts and promising outcomes in medical images analysis, still reproducible and correct segmentation along with abnormalities characterization is a challenging task of brain tumor detection because of its variability in location, shape and size [18,19]. Presenting an automated method to increase tumor detection performance is a motivation of this work. The contributions are as follows:

1. *Lesion enhancement*: Weiner Filter in wavelet domain is employed for noise removal and to enhance lesion region.
2. *Lesion segmentation*: PF clustering method is applied to find out the subset of tumor pixels. Moreover, the global threshold method is used for lesion segmentation. Finally, mathematical morphology is applied for refining the tumor segmentation results.
3. *Feature extraction*: In this phase, GWT and LBP features are obtained through every segmented image and then both texture features are fused to improve discrimination results.

The paper is organized into different sections. Existing work for brain lesions is discussed in Section 2. The presented approach for tumor detection is presented in Section 3 and 4 shows the

achieved outcomes. The conclusion of the presented work is defined in Section 5.

2. Related work

In the past, many approaches are proposed for the detection of tumor using MRI. Abbasi and Tajeripour [20] suggested a method in which preprocessing is performed using histogram matching and bias field correction. Various machine learning techniques are also used for tumor detection using MRI [21,22] including k-means, Fuzzy C-Means (FCM), thresholding, kernel extreme learning machine (KELM) and level set methods. Yamamoto et al. [23] proposed rule based and level set methods for tumor segmentation. Moreover, five shape based and fifteen gray level features are extracted for the classification of 49 slices of MRI. This method achieves 81.5% sensitivity with 2.9 false positive (FP) rate. Discrete wavelet transform (DWT) [24], artificial neural network (ANN) and k-nearest neighbor (KNN) are suggested for brain tumor detection in [25]. This method is tested on T1 weighted MRI [26]. PF segmentation along with ensemble methods is evaluated on Flair images of BRATS 2013 dataset [27].

Lesion enhancement is a very challenging task and more improvement is required in future while decreasing MSE and increasing PSNR [28]. Gliomas are infiltrative due to fuzzy borders, hence it is more difficult to segment the tumor region [18,19].

To overcome the existing limitations, Weiner filter with different wavelet bands is utilized in this work and PF clustering technique is employed to get the subset of tumor pixels. In addition, global threshold with proposed morphological operations are utilized for the detection of gliomas. Moreover, texture features (GWT, LBP) are fused that are more suitable for demarcation between tumor and non-tumor MR slices. The mathematical notations used in this work are mentioned in Table 1.

Table 1
Notations used in this manuscript.

Notation	Description	Notation	Description
MSE	Mean square error	Avg	Average
FG	Foreground	Q	Quality
PSNR	Peak signal to noise ratio	BG	Background
SSIM	Structural similarity index	ζ_p	BG precision
PF	Potential field	λ_p	FG precision
ROI	Region of interest	ER	Error rate
ACC	Accuracy	ζ_c	Background pixels of the proposed technique
SE	Sensitivity	λ_c	Foreground pixels of the proposed technique
SP	Specificity	ζ_{GT}	Background pixels of ground truth
FN	False negative	λ_{GT}	Foreground pixels of ground truth
FP	False positive	I_w	Entire/ whole image
TN	True negative	\oplus	Dilation
TP	True positive	\ominus	Erosion
DSC	Dice similarity coefficient	S	Structuring element
μ	Mean	KNN	k-nearest neighbor
Σ	Variance	LBP	Local binary pattern
C_k	Independent classes		
G	Ground truth		
GWT	Gabor wavelet transform		

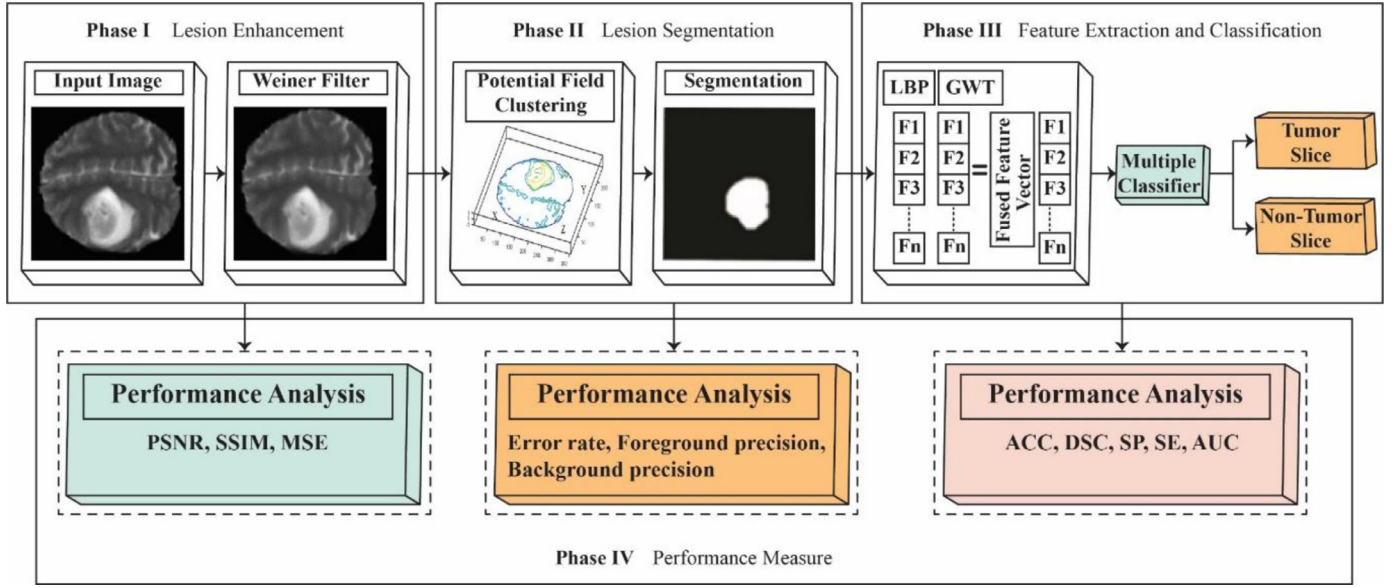


Fig. 2. Proposed method block diagram.

3. Proposed methodology

The presented method for tumor detection is shown in Fig. 2. Wiener filter with different wavelet bands is used for noise reduction and to enhance the region of interest (ROI), PF clustering is applied for segmentation purpose. In addition, an optimal gray level thresholding method is also used. Different texture features are obtained from each segmented slice. Furthermore, multiple classifiers are utilized for separation of MR slices.

3.1. Lesion enhancement

The MR slices contain artifacts such as additional tissues and uneven brightness (e.g., eyes and skull) which minimize overall accuracy. The main challenge in medical slices is noise; hence noise reduction in MR images is a basic step of preprocessing. Although several methods are available for the reduction of noise but they may destroy the details of essential information. That's why Wiener filter is used in this work with different wavelet bands to de-noise the input image $F(u, v)$ and enhance the lesion region to provide better segmentation results. Wiener filtering $G(u, v)$ is used to reduce MSE and can be defined as in Eq. (1).

$$G(u, v) = \frac{H^*(u, v) \text{Spec}_F(u, v)}{|H(u, v)|^2 \text{Spec}_F(u, v) + \text{Spec}_{\text{noise}}(u, v)} \quad (1)$$

Here, $\text{Spec}_F(u, v)$ and $\text{Spec}_{\text{noise}}(u, v)$ represent the power spectrum of input slices and additive noise. $H(u, v)$ denotes low pass filter and H^* shows conjugate of filter. Fig. 3 depicts the lesion enhancement results.

3.2. Segmentation

After lesion enhancement, PF clustering method [27] is used to find the subset of tumor pixels in MRI. The pixels intensity values create PF clustering, for example, finite pixels intensities values are needed to calculate PF clustering at each pixel $f_{(x)}$ that is shown in Fig. 4. PF clustering at $f_{(x)}$ is the sum of individual potentials pixels. In Eq. (2), $\vartheta_y f_{(x)}$ is used to create PF via pixel $f_{(x)}$.

$$\vartheta f_{(x)} = \sum_{y=1}^{\text{number of pixels}} \vartheta_y f_{(x)} \quad (2)$$

XY plane represents equipotential contours.

$$I_g(x, y) = \begin{cases} 1, & \text{if } f(x, y) \leq T \\ 0, & \text{otherwise} \end{cases} \quad (3)$$

$$I_g(x, y) \ominus B = \{\text{vector} \in \text{integer grid} | \text{structuring element}_{\text{vector}} \subseteq g(x, y)\} \quad (4)$$

$$I_g(x, y) = f(x, y) \oplus \text{structuring element} \quad (5)$$

In Eq. (3), the global threshold (T) is applied for brain tumor segmentation. Moreover, morphological erosion with radius 5 disk structuring element is used to remove extra pixels given in Eq. (4). After that, morphological dilation with radius 7 disk structuring element is utilized to recover the missing pixels through Eq. (5). Effects of erosion and dilation are shown in Figs. 5 and 6 while tumor segmentation ($I_{g(x, y)}$) results are shown in Fig. 7. The brain tumor detection algorithm is mentioned below:

Algorithm: Brain tumor segmentation.

```

 $f(x, y)$  = Input slice
 $I_g(x, y)$  = Output slice
 $I_G$  = Gray scale slice
 $I_C$  = Potential field clustering
 $I_E$  = Enhanced slice
 $I_T$  = Tumor segmentation
 $I_{DL} \oplus I_{Er}$  } Morphological operations
Start
Step 1: Input  $\leftarrow f(x, y)$ 
Step 2:  $f(x, y) \leftarrow I_G$  ; ( $I_G \leftarrow \frac{I_{\text{Input}}^R + I_{\text{Input}}^G + I_{\text{Input}}^B}{3}$ )
Step 3:  $I_G \leftarrow I_E$  ; ( $I_E$  = apply Wiener filter)
Step 4:  $I_E \leftarrow I_C$ 
Step 5:  $I_C = I_T = \begin{cases} 1, & \text{if } f(x, y) \leq T \\ 0, & \text{otherwise} \end{cases}$ 
Step 6:  $I_{Er} \leftarrow I_T \ominus \text{structuring element}$ 
Step 7:  $I_{DL} \leftarrow I_{Er} \oplus \text{structuring element}$ 
Step 8:  $I_g(x, y) \leftarrow I_{DL}$ 
End

```

3.3. Features extraction

Features extraction is a vital task to represent an image. In this manuscript, LBP and GWT features are extracted from each

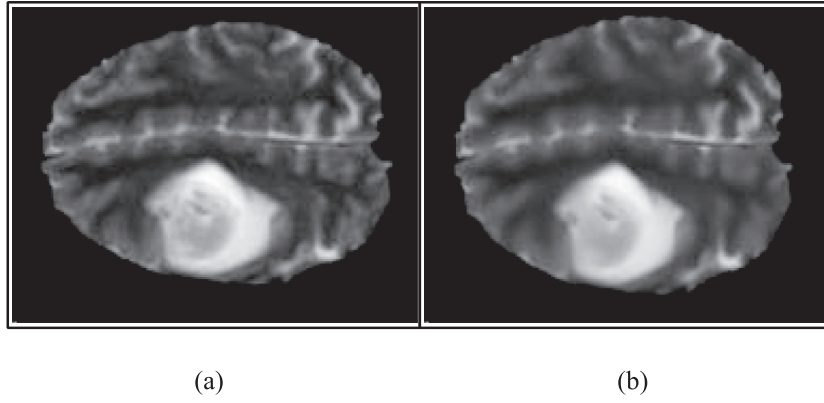


Fig. 3. Lesion enhancement (a) input slice (b) Weiner filter.

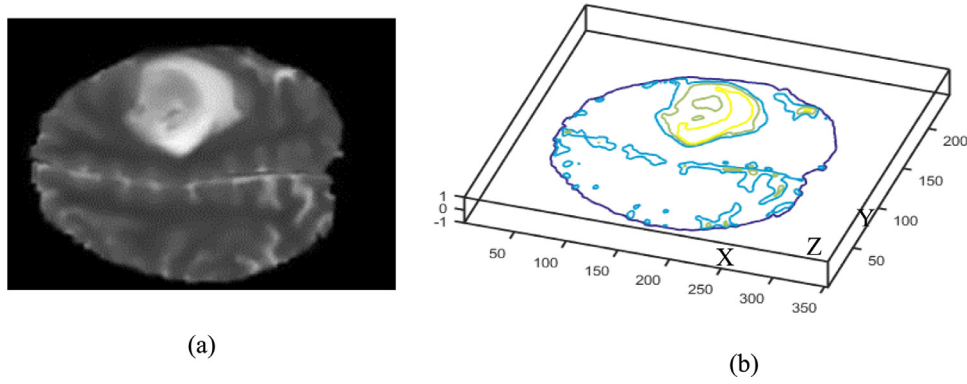


Fig. 4. PF and MRI (a) Brain MRI (b) MRI (x, y, z) denotes the (z) PF at (x, y) pixel in MRI.

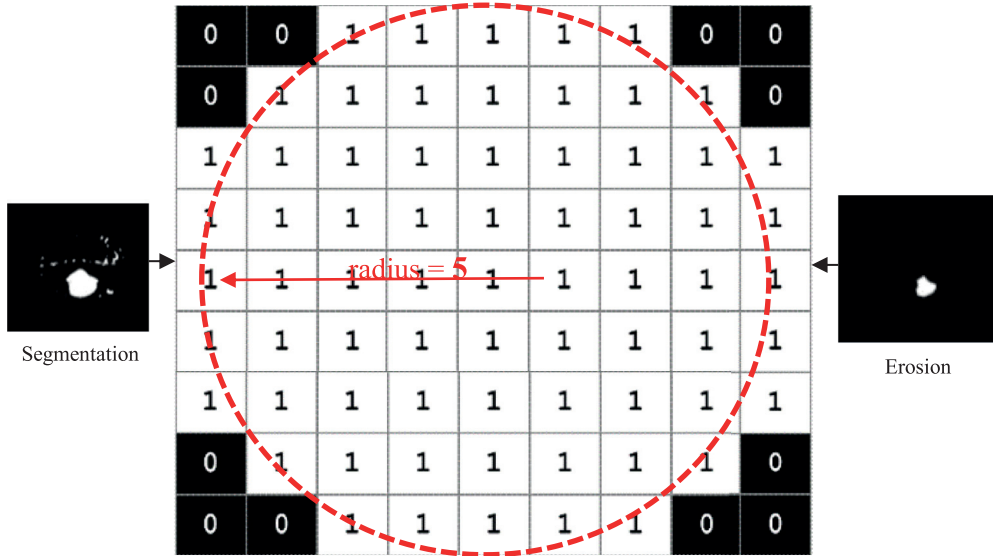


Fig. 5. Morphological erosion on the segmented slice.

segmented slice. Then 50 features are combined into two categories including LBP (30) and GWT (20) features.

3.3.1. Local binary pattern (LBP) features

LBP [29] is extracted from $I_{g(x,y)}$ in which a window slides on the entire slices to compare its neighborhood with central pixel values as a threshold. The neighboring pixel is selected as 1 if it is higher than the center pixel value otherwise 0 value is chosen for the neighboring intensity. Moreover, decimal numbers are assigned

based on binary values. This is given in Eq. (6).

$$LBP_{P,R} = \sum_{i=0}^{P-1} s(g_i - g_c) 2^i s(x) = \begin{cases} 1 & x \geq 0 \\ 0 & x < 0 \end{cases} \quad (6)$$

where P depicts the neighboring pixels, R represents the radius of neighborhood, g_i is neighboring pixels intensity and g_c is central pixel value. The dimension of LBP features is 1×59 .

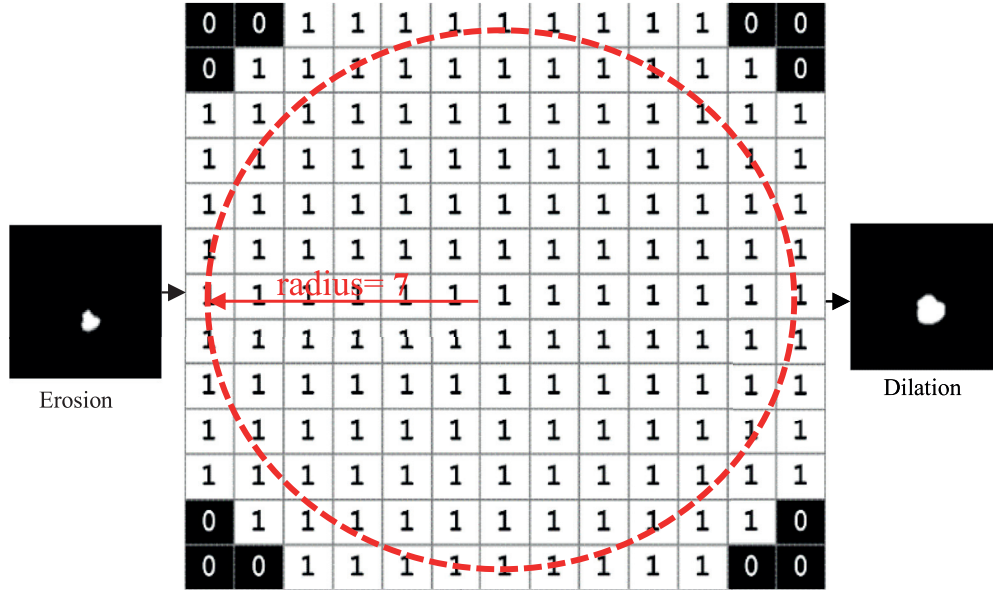


Fig. 6. Morphological dilation of the segmented slice.

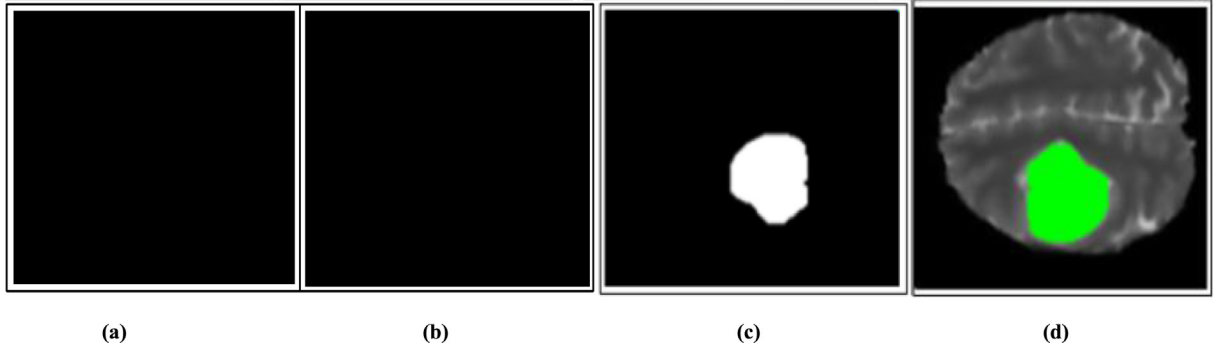


Fig. 7. Results of segmentation (a) after segmentation (b) morphological erosion (c) morphological dilation (d) marking and annotation.

3.3.2. Gabor wavelet transform (GWT) features

GW features consist of a group of Gabor filters (GF) [30] in different directions and frequencies. GF is a Gaussian function that is modulated by using the complex sinusoid. Gabor kernel is mathematically expressed in Eq. (7).

$$\varphi_{u,v}(Z) = \frac{\|k_{u,v}\|}{\sigma^2} \exp\left(-\frac{\|k_{u,v}\|^2 \|Z\|^2}{2\sigma^2}\right) \times \left[\exp(ik_{u,v} Z) - \exp\left(-\frac{\sigma^2}{2}\right) \right] \quad (7)$$

where v, u denote the scale and direction of Gabor kernel, Z shows pixel coordinates in MR slices and can be denoted as $Z=(x, y)$; $\|\dots\|$ stands for the norm process; σ is used to control the Gaussian envelope width; $k_{u,v}=k_v \exp(i\phi_u)$ defines the filter response in different scales and orientations, $k_v = \frac{k_{\max}}{v}$, $\phi_u = \pi u/6$, as described in Fig. 8. Here, k_{\max} shows the peak frequency while f denotes the spacing feature within the frequency domain kernels. The dimension of GWT features is 1×30 .

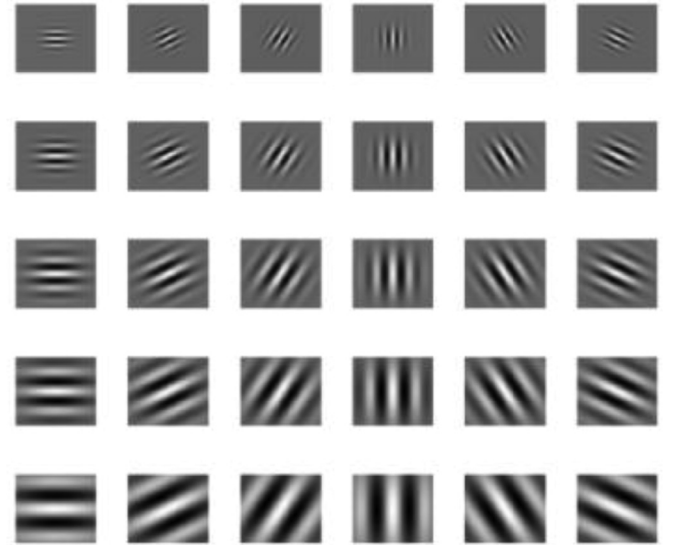


Fig. 8. GWT features to find multi resolution responses.

3.3.3. Proposed fused feature vector

The fused vector (Fv)_{1 × j} is obtained through the concatenation/ fusion (+) of LBP and GWT features by using serial technique [31] based on maximum entropy. Two feature vectors are created as f_{LBP} and f_{SFTA} with $1 \times m$ and $1 \times n$ features dimen-

sions as given in Eqs. (8) and (9).

$$f_{LBP1 \times m} = \{LBP_{1 \times 1}, LBP_{1 \times 2}, LBP_{1 \times 3}, \dots, LBP_{1 \times m}\} \quad (8)$$

$$f_{GWF1 \times n} = \{GWF_{1 \times 1}, GWF_{1 \times 2}, GWF_{1 \times 3}, \dots, GWF_{1 \times n}\} \quad (9)$$

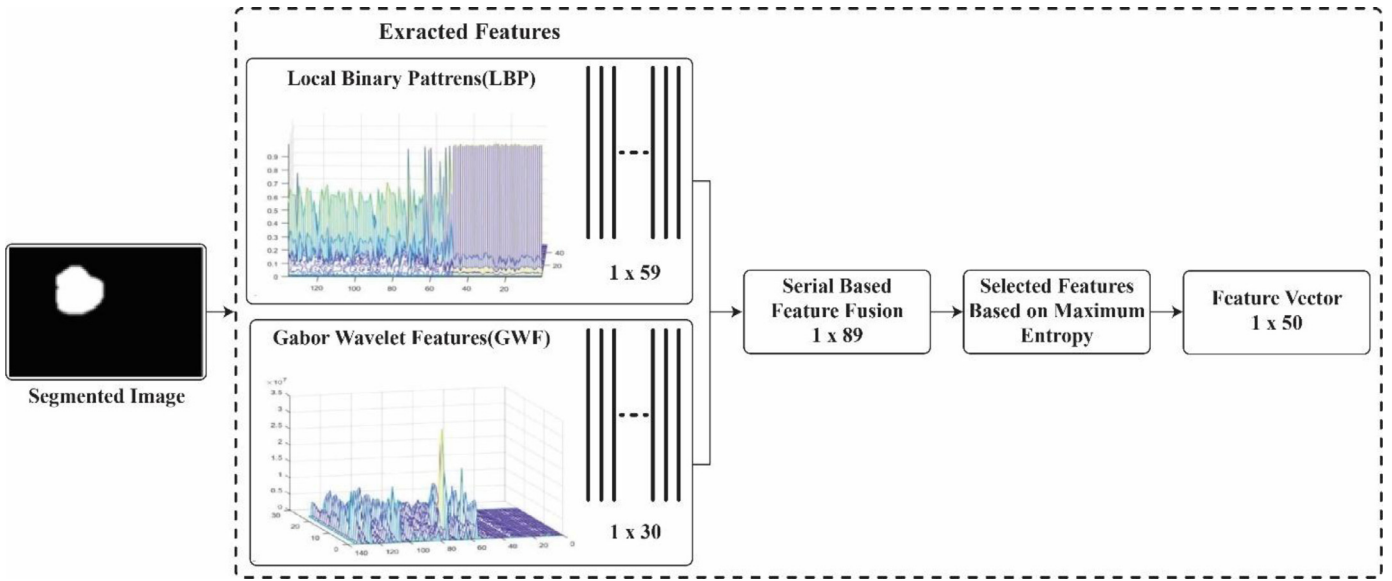


Fig. 9. Features fusion and selection process.

Then extracted features are concatenated/ fused in one vector as presented in Eq. (10).

$$Fv_{1 \times q} = \sum_{i=1}^2 \{fLBP_{1 \times m}, fGWF_{1 \times n}\} \quad (10)$$

where $q \in (m+n)$. The dimension of Fv is 1×89 . The features selection approach based on entropy [32] is applied to each feature vector and most extreme features are chosen dependent on the score [33]. This process is mathematically expressed in Eqs. (11) and (12), where $Fv \in f$ and f represents the fused vector with 1×89 dimension. On the basis of maximum score, 50 features are selected out of 89 features by using Boltzmann entropy (E_b). The overall features fusion process is shown in Fig. 9.

$$\text{Entropy} = -NE_b \sum_{i=1}^n \text{probability}(f_i) \log_2 \text{probability}(f_i) \quad (11)$$

$$F_{\text{selection}} = \text{Entropy}(\max((f_i, 50)) \quad (12)$$

where N denotes total features and n represents the features at similar score level.

3.4. Classification

Multiple classifiers are analyzed with different performance measures on the benchmark datasets to classify segmented slices into tumor/non-tumor. Support vector machine (SVM) is used with quadratic kernel function to perform binary classification task. Subsequently, KNN is utilized with five neighboring elements that are trained to measure the accuracy of classification. Decision Tree (DT) is used on sample data to compute the interdependency attributes based on input data. DT creates a tree structure and assigns attributes and labels on its leaves and edges. Random forest (RF) is a hybrid approach consisting of 200 DT classifiers. Naive Bayes (NB) classifier achieves benefits of independent classes (C_k)

of inter-features association that belongs to the probabilistic family.

4. Experiments and results

The presented technique is checked on two publicly accessible datasets and one locally collected dataset. The local dataset contains 86 images, where 49 tumor and 37 non-tumor images were collected from Nishtar Hospital Multan, Pakistan. BRATS 2013 challenge dataset consists of thirty cases with ground truth annotations in which 20 belong to HG and 10 to LG tumors. BRATS 2015 has 273 cases in which 54 LG and 220 HG gliomas are included. Two modalities (Flair and T2) of each case are utilized for brain tumor detection, where each case has 155 slices of tumor and non-tumor [8,34]. On the basis of ground truth, tumor and non-tumor slices were selected from each case. The detailed description of benchmark datasets is reported in Table 2.

In this work, one experiment is performed for the evaluation of enhancement method and two to evaluate the proposed segmentation technique. The first pixel based experiment is tested on the segmented slice to classify the pixels in term of FG, BG, ER and Q. In the second experiment, classifiers are trained using 10-fold cross validation. All sample slices group into k random subsamples, where one subsample is employed for learning and rest for testing. But the random selection of new sample each time for training and testing can result in the fluctuation of classifiers. Moreover, multiple classifiers performances are discussed in the results section. The experiments are computed on Intel Core i7 with 3.40 GHz using MATLAB 2017a.

4.1. Performance measures

The proposed enhancement technique performance is tested and evaluated with current methods through various measures

Table 2
Description of benchmark datasets.

Database	Modalities	Slices	Cases/ volumes
BRATS 2013 challenge	Flair and T2	Each Flair and T2 has 155 slices in each case	20 HGG and 10 LGG
BRATS 2015 challenge	Flair and T2	Each Flair and T2 has 155 slices in each case	54 LGG and 220 HGG
Local dataset	T2	86 images	49 tumor, 37 non-tumor

Table 3
Enhancement results on benchmark datasets.

	Input slice	PSNR in dB	SSIM	MSE
BRATS 2013	T2-W Axial	76.15	0.986	0.04
	T2-W Axial	75.53	0.985	0.05
	T2-W Axial	76.15	0.988	0.04
	Flair-Axial	76.79	0.989	0.03
	Flair-Axial	76.51	0.990	0.03
BRATS 2015	Flair-Axial	71.13	0.901	0.06
	Flair-Axial	71.03	0.902	0.06
	T2-W Axial	71.52	0.922	0.05
	T2-W Axial	73.67	0.963	0.04
	T2-W Axial	75.58	0.987	0.05
Local dataset	Flair-Axial	71.13	0.901	0.06
	T2-W Axial	74.34	0.977	0.045
	T2-W Axial	77.35	0.994	0.020
	T2-W Axial	76.96	0.994	0.035
	T2-W Axial	76.69	0.992	0.032
	T2-W Axial	76.60	0.992	0.031
	T2-W Axial	74.34	0.977	0.045

such as PSNR, MSE and SSIM. MSE is used to find cumulative error between the original and enhanced slices.

$$MSE = \frac{1}{mn} \sum_{i=0}^{i-1} \sum_{j=0}^{j-1} [f(x, y) - k(x, y)]^2 \quad (13)$$

Less value of MSE is used to facilitate better tumor segmentation results. In the above equation, rows of the original and final images are represented as (i, x) and columns as (j, y). $f(x, y)$ and $k(x, y)$ show the input and enhanced slices [35].

$$PSNR = 10 \log_{10} \left(\frac{MAX_1^2}{MSE} \right) = 20 \log_{20} \left(\frac{MAX_1^2}{\sqrt{MSE}} \right) \\ = 20 \log_{20} (MAX_1) - 10 \log_{10} MSE \quad (14)$$

In Eq. (14), the effect of noise is relatively low with a high value of PSNR. MAX_1 represents maximum pixel value (255) of MR slices.

$$SSIM(x, y) = \frac{(2\mu_x\mu_y + c_1)(2\sigma_{xy} + c_2)}{(\mu_x^2 + \mu_y^2 + c_1)(\sigma_x^2 + \sigma_y^2 + c_2)} \quad (15)$$

SSIM is used for similarity measure among original and enhanced slices. In Eq. (15), σ , μ and c denote variance, mean and contrast respectively.

In addition, performance measures used for the segmentation process are ACC, TPR (known as sensitivity), TNR (known as specificity), AUC, DSC, PPV and Q.

$$ACC = \frac{TP + TN}{TP + TN + FP + FN} \quad (16)$$

$$PPV = \frac{TP}{TP + FP} \quad (17)$$

$$SE = \frac{TP}{TP + FN} \quad (18)$$

$$SP = \frac{TN}{TN + FP} \quad (19)$$

$$AUC = \int_{-\infty}^{\infty} TPR(T)FPR/(T)dT \quad (20)$$

$$DSC = \frac{2TP}{FP + 2TP + FN} \quad (21)$$

$$Q = \frac{|I_{g(x,y)} \cap G|}{|G|} \times \frac{|I_{g(x,y)} \cap G|}{|I_{g(x,y)}|} \quad (22)$$

In Eqs. (16–22), TP, TN, FP and FN are measured through the proposed algorithm. In Eq. (22), G denotes the ground truth image.

Table 4
Enhancement results compared with the existing methods.

Input slice	Algorithm	PSNR in dB	SSIM	MSE
T2-W Axial	[28]	59.39	–	0.074
	[36]	57.34	–	–
FLAIR Axial	Proposed method	76.38	0.98	0.037
	[28]	60.16	–	0.06
	Proposed method	76.20	0.98	0.039

Table 5
Proposed method performance.

Dataset	FG precision	BG precision	ER
Local	0.93	0.98	0.010
BRATS 2013	0.93	0.99	0.005
BRATS 2015	0.97	0.98	0.015

4.2. Experiment#1: enhancement method

The evaluation of enhancement technique is depicted in Table 3 whereas the assessment of presented technique with available approaches is presented in Table 4.

By using the T2-W Axial slice as an input; presented method (uses Weiner filter with different wavelet domain) obtains an average 76.38 PSNR, 0.98 SSIM and 0.037 MSE on T2-W slices. FLAIR slices achieve 76.2 PSNR, 0.98 SSIM and 0.039 MSE. On the same inputs, the method that uses BFO and MFKM [28] for lesion enhancement achieves 60.16 PSNR, 0.06 MSE, 59.39 PSNR and 0.074 MSE on T2-W and FLAIR slices.

4.3. Experiment#2: pixel based results

In this experiment, the presented segmentation approach is evaluated pixel by pixel with ground truth. In the evaluation of pixel based approach, three parameters are considered such as BG Precision (ζ_p), FG precision (λ_p) and error rate (E_R) [37]. To classify pixels related to FG and BG regions, mathematical representation is given in Eqs. (23) and (24).

$$\lambda_p \leftarrow \frac{|\{\lambda_C\} \cap \{\lambda_{GT}\}|}{|\{\lambda_C\}|} \quad (23)$$

$$\zeta_p \leftarrow \frac{|\{\zeta_C\} \cap \{\zeta_{GT}\}|}{|\{\zeta_C\}|} \quad (24)$$

$$E_R \leftarrow \frac{|(\{\lambda_C\} \cap \{\lambda_{GT}\} \cap \{\zeta_C\} \cap \{\zeta_{GT}\})|}{I_w} \quad (25)$$

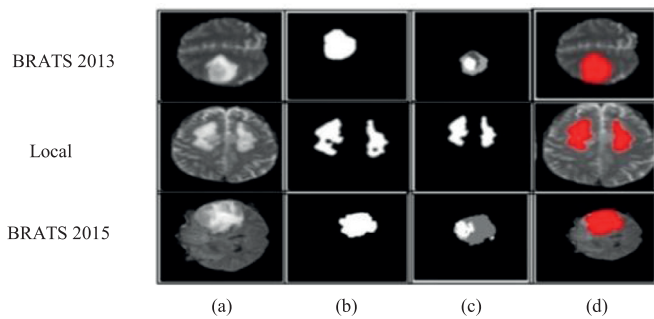
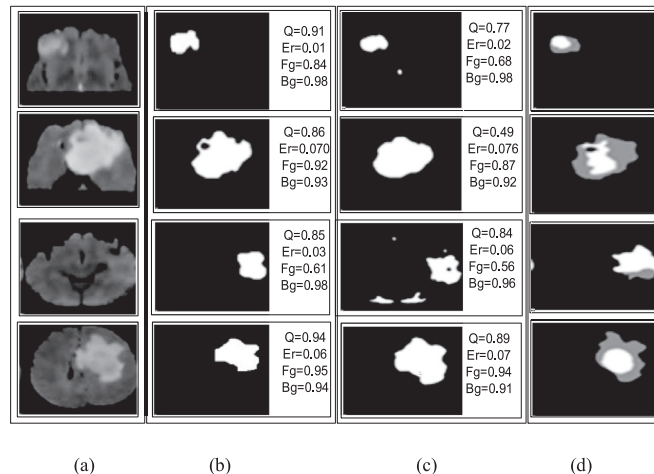
where ζ_C and λ_C denote BG and FG pixels acquired by the proposed approach, ζ_{GT} and λ_{GT} show the ground truth annotations of these pixels and I_w represents the entire slice. ER indicates the degree of misclassified area to the slice size. In order to decide which pixel belongs to which area i.e., FG, BG or ER, threshold values of $T_{FG} = 255 \times 0.95$ and $T_{BG} = 255 \times 0.05$ are applied. When the pixel value is greater than T_{FG} , it is selected as FG pixel and if the pixel value is less than T_{BG} , it is considered as BG pixel. The pixel based results are mentioned in Table 5. Fig. 10 shows some sample results of the presented approach.

The obtained results are as 0.010 ER, 0.93 FG precision and 0.98 BG precision on the local dataset. Similarly, 0.93 FG precision, 0.99 BG precision and 0.005 ER are on BRATS 2013 dataset. On BRATS 2015 dataset, obtained results are 0.97 FG precision, 0.98 BG precision and 0.015 ER. BRATS 2013 achieves better FG precision and minimum ER. Comparison of proposed method with available method [27] is shown in Fig. 11, where the existing method has 0.89 Q while proposed method achieves 0.94 Q.

Table 6

Complete tumor segmented results in cases of BRATS 2013 challenge dataset using flair and T2 modalities.

HGG/ LGG	Cases	Slices	Complete tumor Q	Complete tumor PPV	Complete tumor SE	Complete tumor SP	Complete tumor DSC
HGG slices	brats_2013_pat0001_1	155/155	0.93	0.98	0.99	0.93	0.92
	brats_2013_pat0002_1	155/155	0.98	0.97	0.98	0.92	0.86
	brats_2013_pat0003_1	155/155	0.97	0.94	0.98	0.97	0.87
	brats_2013_pat0004_1	155/155	0.96	0.99	0.97	0.98	0.91
	brats_2013_pat0005_1	155/155	0.92	0.93	0.98	0.95	0.82
	brats_2013_pat0006_1	155/155	0.97	0.96	0.99	0.96	0.95
	brats_2013_pat0007_1	155/155	0.98	0.98	0.97	0.92	0.98
	brats_2013_pat0008_1	155/155	0.94	0.98	0.97	0.96	0.96
	brats_2013_pat0009_1	155/155	0.90	0.98	0.98	0.95	0.84
	brats_2013_pat0010_1	155/155	0.95	0.93	0.98	0.94	0.84
	brats_2013_pat0011_1	155/155	0.95	0.98	0.99	0.91	0.99
	brats_2013_pat0012_1	155/155	0.92	0.99	0.97	0.97	0.83
	brats_2013_pat0013_1	155/155	0.79	0.99	0.98	0.98	0.82
	brats_2013_pat0014_1	155/155	0.93	0.99	0.98	0.8	0.85
	brats_2013_pat0015_1	155/155	0.82	0.96	0.99	0.96	0.81
	brats_2013_pat0022_1	155/155	0.94	0.98	0.99	0.86	0.87
	brats_2013_pat0024_1	155/155	0.93	0.98	0.99	0.92	0.84
	brats_2013_pat0025_1	155/155	0.95	0.99	0.98	0.97	0.93
	brats_2013_pat0026_1	155/155	0.98	0.98	0.97	0.93	0.92
	brats_2013_pat0027_1	155/155	0.97	0.97	0.96	0.92	0.86
LGG slices	brats_2013_pat0001_1	155/155	0.95	0.94	0.98	0.97	0.87
	brats_2013_pat0002_1	155/155	0.85	0.99	0.97	0.98	0.91
	brats_2013_pat0004_1	155/155	0.97	0.92	0.97	0.8	0.84
	brats_2013_pat0006_1	155/155	0.96	0.97	0.98	0.91	0.98
	brats_2013_pat0008_1	155/155	0.99	0.97	0.99	0.9	0.87
	brats_2013_pat0011_1	155/155	0.97	0.91	0.99	0.96	0.82
	brats_2013_pat0012_1	155/155	0.94	0.98	0.98	0.87	0.77
	brats_2013_pat0013_1	155/155	0.96	0.96	0.96	0.93	0.91
	brats_2013_pat0014_1	155/155	0.96	0.97	0.99	0.85	0.84
	brats_2013_pat0015_1	155/155	0.98	0.97	0.97	0.99	0.96
	Average		0.94	0.96	0.97	0.92	0.88

**Fig. 10.** Proposed approach performance (a) input slice (b) results (c) ground truth slices (d) marking/ annotation results.**Fig.11.** Proposed method comparison with the existing techniques (a) input slice (b) proposed segmentation results (c) existing method [27] (d) ground truth annotations.

Based on the performance evaluation, it is observed that when FG precision increases, ER minimizes. As compared to the existing method, presented segmentation method achieves better experimental results. Moreover, pixel based segmentation results are evaluated with ground truth annotations mentioned in Table 6 in which 30 cases of BRATS 2013 are used, where 20 cases belong to HG tumor and 10 cases belong to LG tumor. In each case, four modalities are included but in this manuscript, two modalities such as T2 and Flair are used. Each modality has 155 slices. On the basis of ground truth, Q, DSC, PPV, SE and SP are calculated for each case. In terms of SE, DSC and PPV, the results of this work are compared with [38] in Table 7.

4.4. Experiment#3 (feature based results)

The experiment is performed on the fused feature vector for discrimination between the tumor and non-tumor slices and outcomes are depicted in Tables 8–10. ROC curves of multiple classifiers are presented in Figs. 12–14.

In features extraction step, features from each slice are represented via a row vector. Moreover, class label is assigned to the last element of each row vector. The results depict that KNN performs better and achieves 1.00 AUC and 1.00 ACC when it is applied with an optimized features set. The outcomes are performed on individual LBP and GWT texture features and fused texture features as well. Based on these results, the maximum ACC and AUC of suggested approach are highlighted. On BRATS 2013, average ACC and

Table 7

Comparison of the proposed method results.

Ref	Year	SE	DSC	PPV
[38]	2018	0.84 ± 0.07	0.85 ± 0.02	0.88 ± 0.06
Proposed method		0.97	0.88	0.96

Table 8
Feature based results on BRATS 2013.

Features	Methods	TN	TP	FN	FP	SP	SE	ACC	DSC	AUC
Fused features	SVM	11	70	4	1	0.91	0.94	0.94	0.96	0.97
	NB	14	70	0	2	0.87	1.00	0.97	0.98	0.96
	Ensemble	6	74	6	0	1.00	0.92	0.93	0.96	0.96
	DT	12	71	0	3	0.80	1.00	0.96	0.97	0.97
	KNN	12	74	0	0	1.00	1.00	1.00	1.00	1.00
GWT	RF	13	70	3	0	1.00	0.95	0.96	0.97	0.97
	SVM	9	70	3	4	0.69	0.95	0.91	0.95	0.96
	NB	08	72	1	5	0.61	0.98	0.93	0.96	0.95
	Ensemble	5	72	7	2	0.71	0.91	0.91	0.94	0.89
	DT	11	73	1	1	0.91	0.98	0.97	0.98	0.95
LBP	KNN	12	74	0	0	1.00	1.00	1.00	1.00	1.00
	RF	6	71	5	4	0.60	0.93	0.89	0.94	0.96
	SVM	5	74	7	0	1.00	0.91	0.91	0.95	0.97
	NB	12	70	0	4	0.75	1.00	0.95	0.97	0.96
	Ensemble	6	71	6	3	0.66	0.92	0.89	0.94	0.95
	DT	12	71	3	0	1.00	0.95	0.96	0.97	0.97
	KNN	12	74	0	0	1.00	1.00	1.00	1.00	1.00
	RF	71	10	3	2	0.76	0.97	0.94	0.96	0.97

Table 9
Feature based results on BRATS 2015.

Features	Methods	TN	TP	FN	FP	SP	SE	ACC	DSC	AUC
Fused features	SVM	106	290	0	10	0.91	1.00	0.97	0.98	0.96
	NB	105	296	0	05	0.95	1.00	0.98	0.99	0.99
	Ensemble	50	301	50	5	0.90	0.85	0.86	0.91	0.99
	DT	100	296	0	10	0.90	1.00	0.97	0.98	0.98
	KNN	89	306	11	0	1.00	0.96	0.97	0.98	0.94
GWT	RF	100	295	10	1	0.99	0.96	0.97	0.98	0.99
	SVM	100	296	0	10	0.90	1.00	0.97	0.98	0.96
	NB	100	296	0	10	0.90	1.00	0.97	0.98	0.95
	Ensemble	50	300	50	6	0.89	0.85	0.86	0.91	0.99
	DT	100	296	0	10	0.90	1.00	0.97	0.98	0.99
LBP	KNN	89	306	11	0	1.00	0.96	0.97	0.98	0.94
	RF	99	296	10	1	0.99	0.97	0.97	0.98	0.99
	SVM	100	291	0	15	0.86	1.00	0.96	0.97	0.96
	NB	100	296	0	10	0.90	1.00	0.97	0.98	0.95
	Ensemble	40	306	60	0	1.00	0.83	0.85	0.91	0.99
	DT	100	296	0	10	0.90	1.00	0.97	0.98	0.98
	KNN	89	306	11	0	1.00	0.96	0.97	0.98	0.94
	RF	90	300	3	13	0.87	0.99	0.96	0.97	0.96

Table 10
Feature based results on a local dataset.

Features	Methods	TN	TP	FN	FP	SP	SE	ACC	DSC	AUC
Fused features	SVM	14	70	0	2	0.87	1.00	0.97	0.98	0.80
	NB	17	61	1	7	0.70	0.98	0.90	0.93	0.91
	Ensemble	10	68	6	2	0.83	0.91	0.90	0.95	0.77
	DT	12	69	0	5	0.70	1.00	0.94	0.96	0.96
	KNN	15	69	0	4	0.78	1.00	0.93	0.95	0.96
GWT	RF	10	72	0	4	0.71	1.00	0.95	0.97	0.97
	SVM	24	37	13	12	0.66	0.74	0.70	0.74	0.78
	NB	30	35	7	14	0.68	0.83	0.75	0.76	0.82
	Ensemble	14	45	23	4	0.77	0.66	0.68	0.76	0.90
	DT	33	41	4	8	0.80	0.91	0.86	0.87	0.93
LBP	KNN	37	43	0	6	0.86	1.00	0.93	0.93	0.93
	RF	40	43	3	0	1.00	0.93	0.96	0.96	0.94
	SVM	30	35	10	11	0.73	0.77	0.75	0.76	0.82
	NB	32	31	08	15	0.68	0.79	0.72	0.72	0.84
	Ensemble	17	37	23	9	0.65	0.61	0.62	0.73	0.70
	DT	35	38	5	8	0.81	0.88	0.84	0.85	0.93
	KNN	40	40	0	6	0.86	1.00	0.93	0.93	0.81
	RF	11	66	8	1	0.91	0.89	0.89	0.93	0.92

AUC by using LBP features with SVM are 0.91 and 0.97 respectively. NB achieves 0.95 ACC and 0.96 AUC. The ensemble has 0.89 ACC and 0.95 AUC. DT obtains 0.96 ACC and 0.97 AUC. Similarly, on BRATS 2015, SVM has 0.96 ACC and 0.96 AUC. NB and DT show 0.97 ACC and 0.95 and 0.98 AUC whereas Ensemble presents 0.85 ACC and 0.99 AUC. KNN shows 0.97 ACC and 0.94 AUC respectively.

The experimental results on the proposed fused features by using KNN achieve 1.00 ACC and 1.00 AUC on BRATS 2013 while NB obtains 0.98 ACC and 0.99 AUC on BRATS 2015 and KNN presents 0.93ACC and 0.96 AUC on local dataset respectively. The results show that fused texture features have greater discriminative power as compared to the existing features.

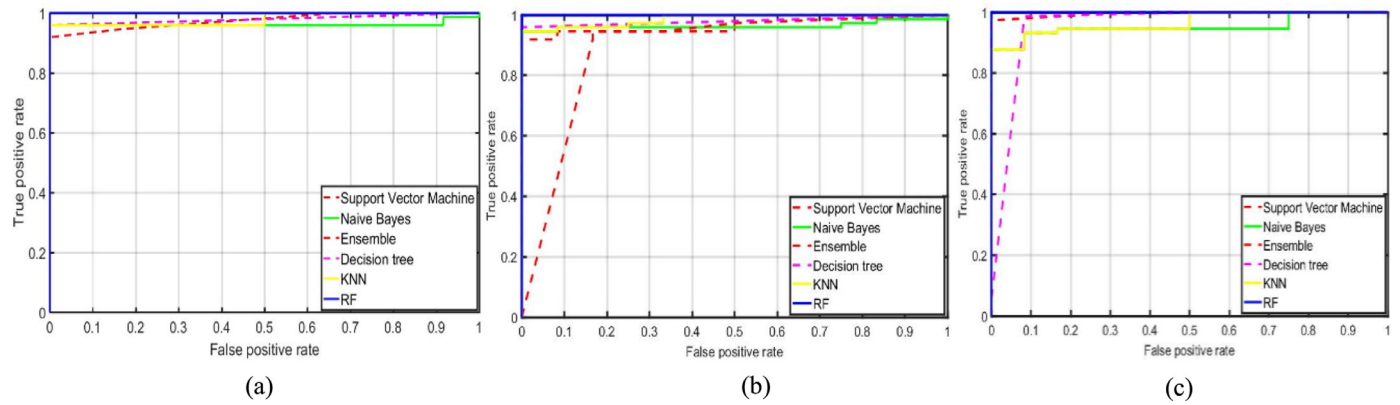


Fig. 12. AUC and ROC analysis by utilizing multiple classifiers trained and tested over proposed features set with 10-fold cross validation on BRATS 2013 (a) fused features (b) GWT features (c) LBP features.

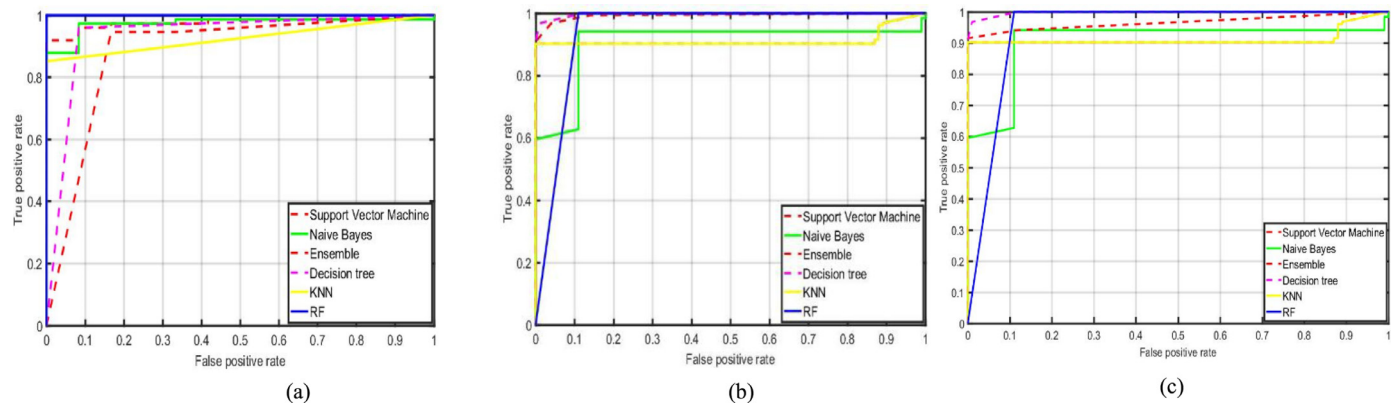


Fig. 13. AUC and ROC analysis by utilizing multiple classifiers trained and tested over proposed features set with 10-fold cross validation on BRATS 2015 (a) fused features (b) GWT features (c) LBP features.

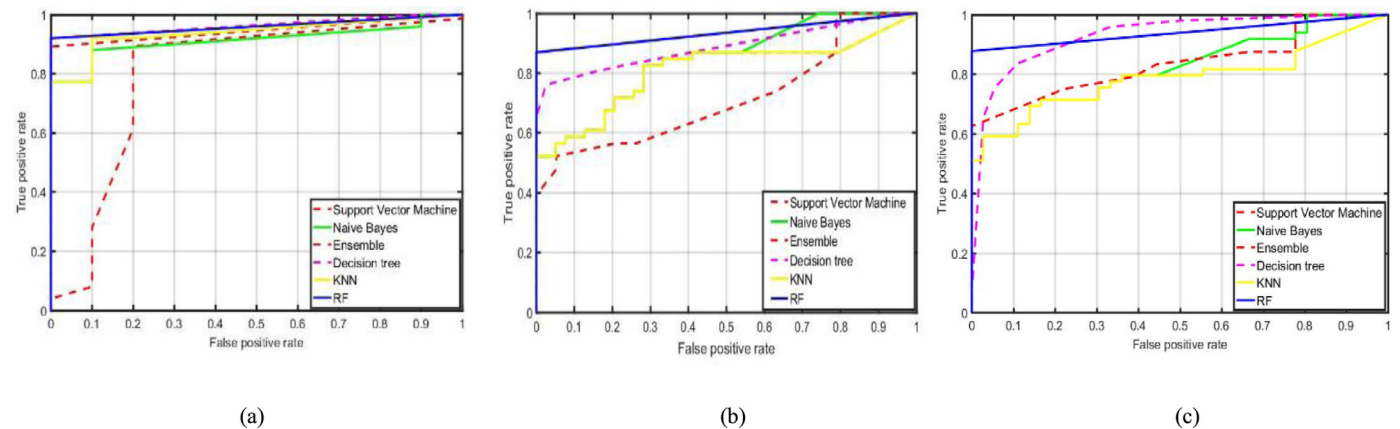


Fig. 14. AUC and ROC analysis by utilizing multiple classifiers trained and tested over proposed features set with 10-fold cross validation on the local dataset (a) fused features (b) GWT features (c) LBP features.

Table 11
Proposed technique comparison with existing methods.

Database	Year	Ref	DSC Complete tumor
BRATS 2013	2016	[40]	0.88
	2017	[39]	0.88
	2018	[38]	0.85 ± 0.02
	Proposed		0.96
BRATS 2015	2017	[41]	0.84
	2018	[43]	0.86
	2019	[44]	0.89
	Proposed		0.98

Classification results by using proposed selected features set are also compared with nine existing methods such as input cascade CNN [39], CNN [40], 3D-CNN+RF [41], U-Net [42], extremely randomized trees [43] and dual force training scheme [44] as given in Table 11.

On the basis of experiments, it is observed that the proposed method performs well in comparison with existing techniques.

5. Conclusion

Detection at an early stage of brain tumor is presented in this article. The major contribution of this research work is an in-depth

focus on enhancement, segmentation and features fusion process. The proposed hybrid texture features from each segmented slice are supplied to multiple classifiers for the classification of tumor /non-tumor MR slices. On the basis of detailed performance evaluation, it is confirmed that features fusion and KNN outperform as compared to other classifiers. The outcomes depict the strength of the proposed method.

The presented technique is applied only on BRATS challenge datasets. In future, the work can be stretched to deep learning approaches for segmentation of sub tumoral region including complete, core and enhance tumor.

Conflict of interest

None.

Supplementary materials

Supplementary material associated with this article can be found, in the online version, at doi:[10.1016/j.cmpb.2019.05.015](https://doi.org/10.1016/j.cmpb.2019.05.015).

References

- [1] A. Kavitha, L. Chitra, R. Kanaga, Brain tumor segmentation using genetic algorithm with SVM classifier, *Int. J. Adv. Res. Electr. Electron. Instrum. Eng.* 5 (3) (2016) 1468–1471.
- [2] T. Logeswari, M. Karnan, An improved implementation of brain tumor detection using segmentation based on hierarchical self organizing map, *Int. J. Comput. Theory Eng.* 2 (4) (2010) 591.
- [3] N.B. Bahadure, A.K. Ray, and H.P. Thethi, Image analysis for MRI based brain tumor detection and feature extraction using biologically inspired BWT and SVM, *Int. J. Biomed. Imaging*, vol. 2017, 2017.
- [4] J. Liu, M. Li, J. Wang, F. Wu, T. Liu, Y. Pan, A survey of MRI-based brain tumor segmentation methods, *Tsinghua Sci. Technol.* 19 (6) (2014) 578–595.
- [5] S. Ytre-Hauge, Preoperative tumor texture analysis on MRI predicts high-risk disease and reduced survival in endometrial cancer, *J. Magn. Reson. Imaging* 48 (6) (2018) 1637–1647.
- [6] G.S. Tandel, A review on a deep learning perspective in brain cancer classification, *Cancers* 11 (1) (2019) 111.
- [7] S. Bauer, R. Wiest, L.-P. Nolte, M. Reyes, A survey of MRI-based medical image analysis for brain tumor studies, *Phys. Med. Biol.* 58 (13) (2013) R97.
- [8] B.H. Menze, The multimodal brain tumor image segmentation benchmark (BRATS), *IEEE Trans. Med. Imaging* 34 (10) (2015) 1993.
- [9] D.S. Giulia Clementi, Alberto Paoluzzi, Università Roma Tre, Giorgio Scorzelli, Valerio Pascucci, Progressive extraction of neural models from high-resolution 3D images of brain, in: *Proceedings of CAD'16*, 2016, pp. 348–351.
- [10] M. Talo, U.B. Baloglu, Ö. Yildirim, U.R. Acharya, Application of deep transfer learning for automated brain abnormality classification using MR images, *Cognit. Syst. Res.* 54 (2019) 176–188.
- [11] K.E. Emblem, Predictive modeling in glioma grading from MR perfusion images using support vector machines, *Magn. Reson. Med.* 60 (4) (2008) 945–952.
- [12] N. Marshkole, B.K. Singh, A. Thoke, Texture and shape based classification of brain tumors using linear vector quantization, *Int. J. Comput. Appl.* 30 (11) (2011) 21–23.
- [13] H. Fujita, Computer-aided diagnosis: the emerging of three CAD systems induced by Japanese health care needs, *Comput. Methods Programs Biomed.* 92 (3) (2008) 238–248.
- [14] K.R. Laukamp, Fully automated detection and segmentation of meningiomas using deep learning on routine multiparametric MRI, *Eur. Radiol.* 29 (1) (2019) 124–132.
- [15] J. Amin, M. Sharif, M. Yasmin, S.L. Fernandes, Big data analysis for brain tumor detection: deep convolutional neural networks, *Future Gener. Comput. Syst.* 87 (2018) 290–297.
- [16] J. Amin, M. Sharif, M. Raza, M. Yasmin, Detection of brain tumor based on features fusion and machine learning, *J. Amb. Intel. Hum. Comput.* (2018) 1–17.
- [17] J. Amin, M. Sharif, M. Yasmin, S.L. Fernandes, A distinctive approach in brain tumor detection and classification using MRI, *Pattern Recognit. Lett.* (2017).
- [18] V. Simi, J. Joseph, Segmentation of glioblastoma multiforme from MR images—A comprehensive review, *Egypt. J. Radiol. Nuclear Med.* 46 (4) (2015) 1105–1110.
- [19] R. Rewari, Automatic tumor segmentation from MRI scans, 1–6, <https://pdfs.semanticscholar.org/b6ff/b7614ce83ebd8c5c95c75e2603d79455b95d.pdf> (Last Accessed May 2019).
- [20] S. Abbasi, F. Tajeripour, Detection of brain tumor in 3D MRI images using local binary patterns and histogram orientation gradient, *Neurocomputing* 219 (2017) 526–535.
- [21] E. Abdel-Maksoud, M. Elmogy, R. Al Awadi, Brain tumor segmentation based on a hybrid clustering technique, *Egypt. Inform. J.* 16 (1) (2015) 71–81.
- [22] D.R. Nayak, R. Dash, X. Chang, B. Majhi, S. Bakshi, Automated diagnosis of pathological brain using fast curvelet entropy features, *IEEE Trans. Sustain. Comput.* (2018) 1–1.
- [23] D. Yamamoto, Computer-aided detection of multiple sclerosis lesions in brain magnetic resonance images: false positive reduction scheme consisted of rule-based, level set method, and support vector machine, *Comput. Med. ImagingGraphics* 34 (5) (2010) 404–413.
- [24] A. Gudigar, U. Raghavendra, T.R. San, E.J. Ciaccio, U.R. Acharya, Application of multiresolution analysis for automated detection of brain abnormality using MR images: a comparative study, *Future Gener. Comput. Syst.* 90 (2019) 359–367.
- [25] E.-S.A. El-Dahshan, T. Hosny, A.-B.M. Salem, Hybrid intelligent techniques for MRI brain images classification, *Digital Signal Process.* 20 (2) (2010) 433–441.
- [26] M. Graña, Computer aided diagnosis system for Alzheimer disease using brain diffusion tensor imaging features selected by Pearson's correlation, *Neurosci. Lett.* 502 (3) (2011) 225–229.
- [27] I. Cabria, I. Gondra, MRI segmentation fusion for brain tumor detection, *Inf. Fusion* 36 (2017) 1–9.
- [28] A. Vishnuvarthanan, M.P. Rajasekaran, V. Govindaraj, Y. Zhang, A. Thiagarajan, An automated hybrid approach using clustering and nature inspired optimization technique for improved tumor and tissue segmentation in magnetic resonance brain images, *Appl. Soft Comput.* 57 (2017) 399–426.
- [29] L. Liu, P. Fieguth, Y. Guo, X. Wang, M. Pietikäinen, Local binary features for texture classification: taxonomy and experimental study, *Pattern Recognit.* 62 (2017) 135–160.
- [30] N. Nabizadeh, M. Kubat, Brain tumors detection and segmentation in MR images: gabor wavelet vs. statistical features, *Comput. Electr. Eng.* 45 (2015) 286–301.
- [31] M. Nasir, M. Attique Khan, M. Sharif, I.U. Lali, T. Saba, T. Iqbal, An improved strategy for skin lesion detection and classification using uniform segmentation and feature selection based approach, *Microscopy Res. Tech.* 81 (6) (2018) 528–543.
- [32] M. Sharif, M.A. Khan, Z. Iqbal, M.F. Azam, M.I.U. Lali, M.Y. Javed, Detection and classification of citrus diseases in agriculture based on optimized weighted segmentation and feature selection, *Comput. Electron. Agric.* 150 (2018) 220–234.
- [33] M. Sharif, M.A. Khan, T. Akram, M.Y. Javed, T. Saba, A. Rehman, A framework of human detection and action recognition based on uniform segmentation and combination of Euclidean distance and joint entropy-based features selection, *EURASIP J. Image Video Process.* 2017 (1) (2017) 89.
- [34] M. Kistler, S. Bonaretti, M. Pfaher, R. Niklaus, P. Büchler, The virtual skeleton database: an open access repository for biomedical research and collaboration, *J. Med. Internet Res.* 15 (11) (2013) e245.
- [35] N. Thomos, N.V. Boulgouris, M.G. Strintzis, Optimized transmission of JPEG2000 streams over wireless channels, *IEEE Trans. Image Process.* 15 (1) (2006) 54–67.
- [36] N. Gupta, P. Bhatele, P. Khanna, Glioma detection on brain MRIs using texture and morphological features with ensemble learning, *Biomed. Signal Process. Control* 47 (2019) 115–125.
- [37] J. Kim, D. Han, Y.-W. Tai, J. Kim, Salient region detection via high-dimensional color transform and local spatial support, *IEEE Trans. Image Process.* 25 (1) (2016) 9–23.
- [38] A. Pinto, S. Pereira, D. Rasteiro, C.A. Silva, Hierarchical brain tumour segmentation using extremely randomized trees, *Pattern Recognit.* 82 (2018) 105–117.
- [39] M. Havaei, Brain tumor segmentation with deep neural networks, *Medical Image Anal.* 35 (2017) 18–31.
- [40] S. Pereira, A. Pinto, V. Alves, C.A. Silva, Brain tumor segmentation using convolutional neural networks in MRI images, *IEEE Trans. Med. Imaging* 35 (5) (2016) 1240–1251.
- [41] K. Kamnitsas, Efficient multi-scale 3D CNN with fully connected CRF for accurate brain lesion segmentation, *Med. Image Anal.* 36 (2017) 61–78.
- [42] H. Dong, G. Yang, F. Liu, Y. Mo, and Y. Guo, Automatic brain tumor detection and segmentation using U-Net based fully convolutional networks, *arXiv:1705.03820*, 2017.
- [43] X. Zhao, Y. Wu, G. Song, Z. Li, Y. Zhang, Y. Fan, A deep learning model integrating FCNNs and CRFs for brain tumor segmentation, *Medical Image Anal.* 43 (2018) 98–111.
- [44] S. Chen, C. Ding, M. Liu, Dual-force convolutional neural networks for accurate brain tumor segmentation, *Pattern Recognit.* 88 (2019) 90–100.